

Critical quantum metrology robust against dissipation and non-adiabaticity

Jia-Hao Lü,^{1,*} Wen Ning,^{1,*} Fan Wu,^{1,*} Ri-Hua Zheng,¹ Ken Chen,¹
Xin Zhu,¹ Zhen-Biao Yang,^{1,2,†} Huai-Zhi Wu,^{1,‡} and Shi-Biao Zheng^{1,2,§}

¹*Fujian Key Laboratory of Quantum Information and Quantum Optics,
College of Physics and Information Engineering,
Fuzhou University, Fuzhou, Fujian 350108, China*

²*Hefei National Laboratory, Hefei 230088, China*

(Dated: March 8, 2024)

Critical systems near quantum phase transitions were predicted to be useful for improvement of metrological precision, thanks to their ultra-sensitive response to a tiny variation of the control Hamiltonian. Despite the promising perspective, realization of criticality-enhanced quantum metrology is an experimentally challenging task, mainly owing to the extremely long time needed to encode the signal to some physical quantity of a critical system. We here circumvent this problem by making use of the critical behaviors in the Jaynes-Cummings model, comprising a single qubit and a photonic resonator, to which the signal field is coupled. The information about the field amplitude is encoded in the qubit's excitation number in the dark state, which displays a divergent changing rate at the critical point. The most remarkable feature of this critical sensor is that the performance is insensitive to the leakage to bright eigenstates, caused by decoherence and non-adiabatic effects. We demonstrate such a metrological protocol in a superconducting circuit, where an Xmon qubit, interacting with a resonator, is used as a probe for estimating the amplitude of a microwave field coupled to the resonator. The measured quantum Fisher information exhibits a critical quantum enhancement, confirming the potential of this system for quantum metrology.

The capability of accurately measuring a weak signal is crucial for advancing modern science and technology, exemplified by the detection of gravitational waves [1], which not only provides a direct evidence for the validity of general relativity, but also lays the experimental foundation for gravitational-wave astronomy. Quantum metrology aims to exploit quantum sources to improve the precision of measurement of special physical quantities, including the amplitude of a magnetic or electric field, the frequency of an oscillator, and the magnitude of a force [2, 3]. In conventional quantum metrological protocols, the signal is encoded in a quantum superposition of two components with highly distinct quantum numbers for a single element [4–6], e.g. Fock states $|0\rangle$ and $|N\rangle$ of a bosonic mode, or in a highly entangled state for many qubits [7–10]. With such encoding protocols, the achievable sensitivity can exhibit a scaling surpassing the standard quantum limit in principle. However, the vulnerability of these nonclassical states restricts their metrological practicalities, as the gain from the increase of the system size is quickly cancelled out by the environment-induced decoherence effects [11].

Quantum critical phenomena represent an alternative quantum resource for realizing quantum sensing. When a quantum system evolves near the critical point of a phase transition [12], its properties exhibit dramatic changes in response to a slight variation of the governing Hamiltonian. These phenomena are useful for realizing criticality-enhanced quantum sensors [13–40], which aim to exploit critical systems to amplify the effects of the signal fields. In conventional critical metrological protocols [13–32], the physical quantity is encoded in one specific eigenstate of the control Hamiltonian that is adi-

abatically steered towards the critical point. Benefitting from the adiabatic nature, this approach bears an intrinsic robustness against noises. However, it is an experimental challenge to meet the adiabatic condition close to a quantum phase transition, owing to the critical slowing down. To make a quantum system adiabatically follow one specific eigenstate, the changing rate of the control parameter usually needs to be much lower than the corresponding energy gaps. At the phase transition, these gaps vanish, which indicate the probability of leaking to other eigenstates is non-negligible when the system is approaching the critical point within a limited time. This inherent state leakage challenges the practical usefulness of such protocols. Recent theoretical investigations show that the adiabatic condition can be removed with dynamical approaches [30, 38–40], where the parameter to be estimated is encoded in the time-evolving state under a time-independent Hamiltonian, to which the physical quantity of interest is coupled. However, such dynamical protocols also require extremely long evolution time [41], furthermore, their performances depend on precise timing.

We here propose and demonstrate a critical quantum metrological protocol, where the process to bring the system towards the critical point is significantly speeded up, but without loss of the robustness associated with adiabatic evolution. The sensor is composed of a single qubit and a photonic mode interacting with each other, referred to as the Jaynes-Cummings model (JCM) [42]. The signal field, whose amplitude is to be probed, couples to the bosonic mode, producing a continuous drive. Below the critical point, the system has a unique dark state, in which the signal is encoded. The energy gaps

between this dark state and the nearest bright states are continually narrowed when approaching the critical point, where the average excitation numbers for both the photonic mode and the qubit exhibit diverging changing rates. The qubit excitation number, which serves as a robust indicator for estimating the amplitude of the signal field, approaches the same value of $1/2$ near the critical point, no matter whether or not the system is in the dark state. This makes the protocol insensitive to state leakage. We demonstrate this criticality-enhanced metrology with a circuit quantum electrodynamics (QED) system, where a superconducting qubit and a microwave resonator form the JCM. The experimental results unambiguously demonstrate the robustness of the critical quantum sensing protocol.

The theoretical model under consideration involves a photonic mode resonantly interacting with a qubit and driven by a signal field, whose amplitude is to be estimated, as schematically shown in Fig. 1(a). In the interaction picture, the system dynamics is described by the driven JCM (setting $\hbar = 1$) [43]

$$H = \Omega[a^\dagger |g\rangle \langle e| + a |e\rangle \langle g|] + \varepsilon(a^\dagger + a)/2, \quad (1)$$

where a^\dagger and a denote the photonic creation and annihilation operators, $|g\rangle$ and $|e\rangle$ are the ground and excited state of the qubit, Ω represents the qubit-boson interaction strength, and ε characterizes the rescaled amplitude of the signal field coupled to the photonic mode. When $\varepsilon < 1$, the system possesses discrete eigenenergies, given by

$$\begin{aligned} E_0 &= 0, \\ E_{n,\pm} &= \pm\sqrt{n}\Omega A^{3/4}, \end{aligned} \quad (2)$$

where $A = 1 - \varepsilon^2$, as depicted in Fig. 1(b). We note that the eigenenergies are derived in the framework rotating at the frequency of the signal field, and will refer to them as quasi-energies [43]. The corresponding eigenstates are

$$\begin{aligned} |\psi_0\rangle &= S(r)|0\rangle|\phi_0\rangle, \\ |\psi_{n,\pm}\rangle &= S(r)D(\alpha_{n,\pm})(|n-1\rangle|\phi_1\rangle \pm |n\rangle|\phi_0\rangle)/\sqrt{2}, \end{aligned} \quad (3)$$

where $|n\rangle$ denotes the n -photon state, and $S(r)$ and $D(\alpha_{n,\pm})$ are respectively the squeezing and displacement operators for the photonic field, with $r = \frac{1}{4} \ln A$ and $\alpha_{n,\pm} = \mp\sqrt{n}\varepsilon$. $|\phi_\pm\rangle$ denote qubit parts, given by

$$\begin{aligned} |\phi_0\rangle &= c_+ |g\rangle - c_- |e\rangle, \\ |\phi_1\rangle &= c_+ |e\rangle - c_- |g\rangle, \end{aligned} \quad (4)$$

with $c_\pm = (1 \pm \sqrt{A})^{1/2}/\sqrt{2}$. The results show that when the driving strength is increased, the quasi-energy splittings are continually narrowed, all vanishing at the critical point $\varepsilon = 1$, beyond which the quasi-energy spectrum becomes continuous. The quasi-energy level configuration can also be interpreted in terms of the competition

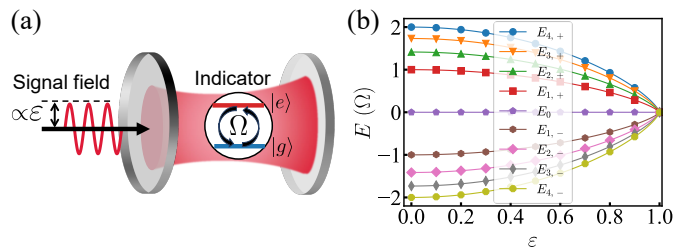


FIG. 1. (color online). Critical quantum sensing protocol. (a) Theoretical model. The model comprises a cavity mode interacting with the transition between the lower ($|g\rangle$) and upper state ($|e\rangle$) of a qubit, with the photonic swapping strength Ω . The signal field with an unknown rescaled amplitude ε is coupled to the resonator. (b) Quasi-energy spectrum. Such a model exhibits a highly nonlinear quasi-energy spectrum, with $E_0 = 0$ and $E_{n,\pm} = \pm\sqrt{n}\Omega(1 - \varepsilon^2)^{3/4}$. When $\varepsilon \ll 1$, the excitation number in the adiabatically evolved dark state is negligible, as a consequence of the photon blockade. At $\varepsilon = 1$ quasi-energy gaps vanish, leading to the breakdown of the photon blockade. Near this critical point, both the photon number and qubit excitation number exhibit a diverging changing rate in response to the variation of ε .

between the JC coupling and the external driving. When the JC coupling dominates over the external driving, the system features the JC-like ladder, manifested by the \sqrt{n} -dependent splitting. If the external driving is dominant, the photonic mode is disentangled with the anharmonic qubit and the spectrum becomes a continuum. This spectral feature is associated with the dissipative-driven photon-blockade breakdown phase transition [44, 45].

We consider the system behaviors below but close to the critical point $\varepsilon = 1$. The associated average photon number, $\langle N \rangle_0 = \sinh^2 r$, displays a divergent behavior and thus can be used as a critical sensing indicator in principle. However, it is sensitive to leakage to the bright states $|\psi_{n,\pm}\rangle$, whose average photon number, $\langle N \rangle_n = 2n\varepsilon^2 e^{-2r} + n \cosh 2r - \frac{1}{2}$, is significantly distinct from that of the dark state. This sensitivity is unfavorable to improvement of the signal-to-noise ratio. In distinct contrast, when $\varepsilon \rightarrow 1$ the qubit excitation number tends to $1/2$, no matter which eigenstate the system is in. This implies that the qubit's excitation number is insensitive to leakage to the bright states, which can be caused either by decoherence or by the non-adiabatic effects. Due to this insensitivity, the qubit's excitation number can be used as a robust indicator for estimating the amplitude of the external drive.

In our sensing protocol, the signal is encoded in the time-evolving eigenstate $|\psi_0\rangle$, which is separated from its nearest eigenstates by $E_{G,\min} = \Omega A^{3/4}$. The ratio between this energy gap and the ramping rate of the control parameter ε determines how well the system can be kept in the dark state. The lower this ramping rate, the smaller the leakage probability to the bright eigenstates.

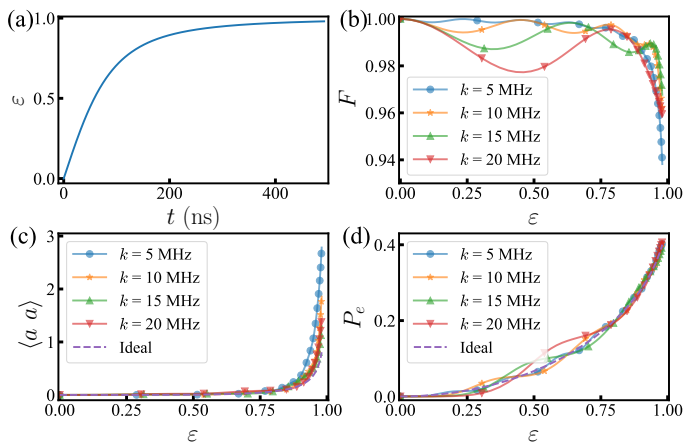


FIG. 2. (color online). Simulations of the quench process. (a) ε versus t . Here ε is varied according to Eq. (5) with $k = 10$ MHz. (b) Fidelities of the qubit-resonator state to the ideal dark state as functions of ε . In the simulation, the qubit-resonator coupling strength is set to $\Omega = 2\pi \times 20.9$ MHz, and the dissipation rates for the qubit and resonator are 0.05 MHz and 0.08 MHz, respectively. (c) Average photon number of the resonator and (d) qubit's excitation number versus ε for different k . The dashed lines in (c) and (d) denote the results for the ideal dark state.

However, a longer evolution time would result in more serious decoherence effects. As a compromise between the non-adiabaticity and decoherence, the dependence of ε on t is modeled as

$$\varepsilon = \sqrt{1 - (k^2 t^2 + 1)^{-1}}, \quad (5)$$

where k is the coefficient controlling the ramping velocity. To clearly show how well the system is restricted to the dark state during the ramping of the control parameter ε , we perform a simulation of the fidelity (F) as a function of ε . Here the fidelity is defined as $F = \langle \psi_0 | \rho | \psi_0 \rangle$, where ρ denotes the density operator for the system, calculated by the master equation with the Hamiltonian Eq. (1). In the simulation, the qubit-resonator coupling strength and the energy dissipative rates are set to be the same as those in our experimental system. The ramping-velocity-controlling parameter is set to $k = 10$ MHz. With this choice, the rescaled field amplitude ε , plotted as a function of t , is shown in Fig. 2(a). Fig. 2(b) shows the simulated evolution of the fidelity relative to the ideal dark state. The infidelity is caused by the leakage to bright states via decoherence and non-adiabatic transitions.

As analyzed above, the average photon number is very sensitive to the state leakage. To provide quantitative evidence for this sensitivity, we simulate the photon-number evolutions during quench process. The result is shown in Fig. 2(c), which confirms that even a slight leakage to the bright states can cause a significant deviation of the average photon number from that in the

dark state. In contrast, the evolution of the qubit's $|e\rangle$ -state population (P_e) is robust against the state leakage, as shown in Fig. 2(d). As expected, when approaching the critical point, P_e calculated with different ramping velocities converge to that of the ideal dark eigenstate. This robustness is due to the fact that at the critical point, each of the bright states is a product state, where the qubit part is the same as in the dark state. Consequently, the evolution of P_e is robust against dissipation, non-adiabaticity, and imperfect timing. More importantly, near the critical point P_e almost displays the same dependence on ε for a quite wide range of k . This allows the problem associated with critical slowing down to be largely compensated by increasing k . For example, for the choice of $k = 10$ MHz, the ramping of ε from 0 to 0.98 is accomplished within a time $T \approx 500$ ns, which is much shorter than the energy relaxation times for the qubit and the photonic mode of the experimental system, $T_1^q = 20 \mu\text{s}$ and $T_1^p = 12 \mu\text{s}$. With this choice, the dependence of P_e on ε well coincides with that for the ideal dark state within the regime $0.8 < \varepsilon < 0.98$. These robustnesses make P_e serve as an ideal indicator for critical quantum sensing.

The critical system is realized in a circuit QED architecture, which involves a bus resonator with a fixed frequency $\omega_r/2\pi \simeq 5.584$ GHz and five frequency-tunable Xmon qubits, one of which is used as the test qubit. The test qubit has an anharmonicity of $\chi \simeq 2\pi \times 0.245$ GHz. The on-resonance photonic swapping rate between the qubit and the resonator is $\Omega \simeq 2\pi \times 20.9$ MHz. The energy decaying rates for the qubit and the resonator are $\kappa_q \simeq 0.05$ MHz and $\kappa_r \simeq 0.08$ MHz, respectively. The dephasing rate of the qubit, measured at its idle frequency is around 1.25 MHz. We note that the dephasing noises are highly suppressed by resonantly coupling to the photonic field, as a consequence of the dynamical decoupling [46].

Before the experiment, the test qubit is initialized to its ground state at the idle frequency $\omega_0/2\pi = 5.35$ GHz, where it is effectively decoupled from the bus resonator since the corresponding detuning is much larger than Ω . The interaction between this qubit and the resonator is activated by tuning the qubit to the resonator's frequency. At the same time, the signal field with a rescaled amplitude ε is coupled to the resonator, continuously driving the photonic field. The experimental pulse sequence ε versus t is set to be the same as that shown in Fig. 2(a).

Due to the limited anharmonicity, the Xmon has a probability of leaking to levels higher than $|e\rangle$, which increases with the resonator's photon number. To suppress this leakage, we fine tune the detunings of the qubit and the resonator (see Supplemental Material). When ε reaches a preset value, the qubit is biased back to its idle

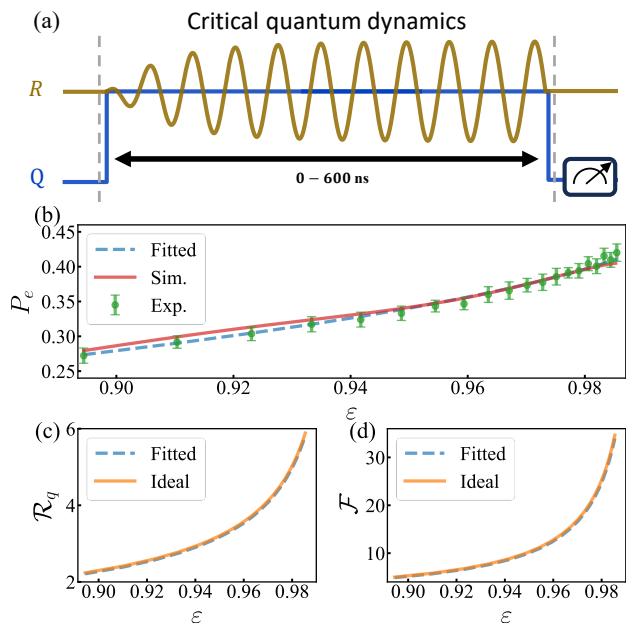


FIG. 3. (color online). Performance of the criticality-enhanced sensing. (a) Pulse sequence. The qubit (Q) is tuned from its idle frequency to the resonator's frequency. At the same time the signal field with a rescaled amplitude ε is coupled to the resonator. After the quench process, the qubit is biased back to its idle frequency for state readout. ε is the time-dependent function shown in Fig. 2(a). (b) Qubit's $|e\rangle$ -state population measured versus ε . The solid line denotes the simulation including the second-excited state of the Xmon, and the dashed line is the fitted function $P_e = C(1 - \sqrt{1 - \varepsilon^2})/2$, with $C = 0.9899$. (c) Signal-to-noise ratio (\mathcal{R}_q) and (d) Fisher information \mathcal{F} versus ε . The solid lines in (c) and (d) are the ideal results based on the adiabatic evolution of the dark state.

frequency for state readout. The qubit's $|e\rangle$ -state populations, measured for different values of ε , are displayed in Fig. 3(b). The measured data well agree with the numerical simulation, where the Xmon's second-excited state $|f\rangle$ is included. The slight fluctuations are mainly caused by imperfect calibration of the amplitude of the signal field. In our experiment, ε is calibrated by coupling the signal field to the resonator for a given time, and then reading out the resonator's average photon number with an ancilla qubit (see Supplemental Material). The errors in this procedure make the calibrated value of ε deviate from the real value. The dashed line denotes the function $C(1 - \sqrt{A})/2$, fitted with the data measured within the range $0.9 < \varepsilon < 0.985$, where the fitted parameter C is 0.9899, close to the ideal value $C = 1$. This agreement confirms that the critical behaviors of the qubit are well controlled.

The critical enhancement is manifested by the diverging changing rate of P_e in the dark state $|\psi_0\rangle$, given by $dP_e/d\varepsilon = \varepsilon/(2\sqrt{A})$, which tends to $1/[2\sqrt{2(1 - \varepsilon)}]$ when $1 - \varepsilon \ll 1$. Consequently, in proximity of the critical

point, a tiny variation of ε would result in dramatic responses of the qubit. The signal-to-noise ratio is given by

$$\mathcal{R}_q = \frac{dP_e/d\varepsilon}{\Delta P_e}, \quad (6)$$

where $\Delta P_e = \varepsilon/2$ denotes the standard deviation for measuring P_e (see Supplemental Material). In proximity of the critical point, \mathcal{R}_q is approximately given by $1/\sqrt{2(1 - \varepsilon)}$. \mathcal{R}_q versus ε [inferred from ε -dependence of P_e in Fig. 3(b)] is shown in Fig. 3(c). The performance of the quantum sensor can be further quantified by the Fisher information, defined as

$$\mathcal{F} = \frac{1}{P_e} \left(\frac{dP_e}{d\varepsilon} \right)^2 + \frac{1}{P_g} \left(\frac{dP_g}{d\varepsilon} \right)^2. \quad (7)$$

As shown in the Supplemental Material, \mathcal{F} is equal to the quantum Fisher information, thereby saturating the Cramér-Rao bound. Fig. 3(d) presents the Fisher information evolution (dashed line) obtained also from the fitted P_e . Within the range $0.9 < \varepsilon < 0.985$, the results for \mathcal{R}_q and \mathcal{F} both agree well with those calculated with the ideal dark state (solid lines).

In conclusion, we have theoretically proposed and experimentally demonstrated a scheme for realizing a criticality-enhanced quantum sensing protocol. The critical system comprises a qubit and a photonic field stored in a resonator. Under the driving of the signal field, the system has a unique dark eigenstate, where the qubit's excitation number is used as the indicator for estimating the signal field amplitude. The performance of the sensor is insensitive to leakage to the bright states, caused by non-adiabaticity and dissipation, as the qubit is in the same state at the critical point, no matter the system is in the dark or bright states. We demonstrate our critical sensing protocol with a circuit QED architecture. Our approach can be directly applied to other spin-boson systems, e.g., ion traps, paving the way to exploit critical phenomena for quantum metrological applications.

This work was supported by the National Natural Science Foundation of China under (Grants No. 12274080, No. 12174058, No. 11875108, No. 12204105), and Innovation Program for Quantum Science and Technology under Grant No. 2021ZD0300200.

* These authors equally contributed to the work.

† zbyang@fzu.edu.cn

‡ huaizhi.wu@fzu.edu.cn

§ t96034@fzu.edu.cn

- [1] B. P. A. et al. (LIGO Scientific and Virgo Collaborations), Observation of gravitational waves from a binary black hole merger, *Phys. Rev. Lett.* **116**, 061102 (2016).
- [2] C. L. Degen, F. Reinhard, and P. Cappellaro, Quantum sensing, *Rev. Mod. Phys.* **89**, 035002 (2017).

- [3] D. Braun, G. Adesso, F. Benatti, R. Floreanini, U. Marzolino, M. W. Mitchell, and S. Pirandola, Quantum-enhanced measurements without entanglement, *Rev. Mod. Phys.* **90**, 035006 (2018).
- [4] A. Facon, E.-K. Dietsche, D. Grosso, S. Haroche, J.-M. Raimond, M. Brune, and S. Gleyzes, A sensitive electrometer based on a Rydberg atom in a Schrödinger-cat state, *Nature (London)* **535**, 262 (2016).
- [5] K. C. McCormick, J. Keller, S. C. Burd, D. J. Wineland, A. C. Wilson, and D. Leibfried, Quantum-enhanced sensing of a single-ion mechanical oscillator, *Nature (London)* **572**, 86 (2019).
- [6] W. Wang, Y. Wu, Y. Ma, W. Cai, L. Hu, X. Mu, Y. Xu, Z.-J. Chen, H. Wang, Y. P. Song, H. Yuan, C.-L. Zou, L.-M. Duan, and L. Sun, Heisenberg-limited single-mode quantum metrology in a superconducting circuit, *Nat. Commun.* **10**, 4382 (2019).
- [7] T. Nagata, R. Okamoto, J. L. O'Brien, K. Sasaki, and S. Takeuchi, Beating the standard quantum limit with four-entangled photons, *Science* **316**, 726 (2007).
- [8] D. Leibfried, M. D. Barrett, T. Schaetz, J. Britton, J. Chiaverini, W. M. Itano, J. D. Jost, C. Langer, and D. J. Wineland, Toward heisenberg-limited spectroscopy with multiparticle entangled states, *Science* **304**, 1476 (2004).
- [9] T. Monz, P. Schindler, J. T. Barreiro, M. Chwalla, D. Nigg, W. A. Coish, M. Harlander, W. Hänsel, M. Heinrich, and R. Blatt, 14-qubit entanglement: Creation and coherence, *Phys. Rev. Lett.* **106**, 130506 (2011).
- [10] G. P. Greve, C. Luo, B. Wu, and J. K. Thompson, Entanglement-enhanced matter-wave interferometry in a high-finesse cavity, *Nature (London)* **610**, 472 (2022).
- [11] L. Pezzè, Y. Li, W. Li, and A. Smerzi, Witnessing entanglement without entanglement witness operators, *Proc. Natl. Acad. Sci. U.S.A.* **113**, 11459 (2016).
- [12] S. Sachdev, *Quantum Phase Transitions*, 2nd ed. (Cambridge University Press, 2011).
- [13] P. Zanardi and N. Paunković, Ground state overlap and quantum phase transitions, *Phys. Rev. E* **74**, 031123 (2006).
- [14] A. F. Albuquerque, F. Alet, C. Sire, and S. Capponi, Quantum critical scaling of fidelity susceptibility, *Phys. Rev. B* **81**, 064418 (2010).
- [15] T.-L. Wang, L.-N. Wu, W. Yang, G.-R. Jin, N. Lambert, and F. Nori, Quantum fisher information as a signature of the superradiant quantum phase transition, *New J. Phys.* **16**, 063039 (2014).
- [16] W.-L. You, Y.-W. Li, and S.-J. Gu, Fidelity, dynamic structure factor, and susceptibility in critical phenomena, *Phys. Rev. E* **76**, 022101 (2007).
- [17] P. Zanardi, M. G. A. Paris, and L. Campos Venuti, Quantum criticality as a resource for quantum estimation, *Phys. Rev. A* **78**, 042105 (2008).
- [18] M. Tsang, Quantum transition-edge detectors, *Phys. Rev. A* **88**, 021801 (2013).
- [19] C. Invernizzi, M. Korbman, L. Campos Venuti, and M. G. A. Paris, Optimal quantum estimation in spin systems at criticality, *Phys. Rev. A* **78**, 042106 (2008).
- [20] S. Gammelmark and K. Mølmer, Phase transitions and heisenberg limited metrology in an ising chain interacting with a single-mode cavity field, *New J. Phys.* **13**, 053035 (2011).
- [21] P. A. Ivanov and D. Porras, Adiabatic quantum metrology with strongly correlated quantum optical systems, *Phys. Rev. A* **88**, 023803 (2013).
- [22] G. Salvatori, A. Mandarino, and M. G. A. Paris, Quantum metrology in lipkin-meshkov-glick critical systems, *Phys. Rev. A* **90**, 022111 (2014).
- [23] M. Bina, I. Amelio, and M. G. A. Paris, Dicke coupling by feasible local measurements at the superradiant quantum phase transition, *Phys. Rev. E* **93**, 052118 (2016).
- [24] M. M. Rams, P. Sierant, O. Dutta, P. Horodecki, and J. Zakrzewski, At the limits of criticality-based quantum metrology: Apparent super-heisenberg scaling revisited, *Phys. Rev. X* **8**, 021022 (2018).
- [25] S. Wald, S. V. Moreira, and F. L. Semião, In- and out-of-equilibrium quantum metrology with mean-field quantum criticality, *Phys. Rev. E* **101**, 052107 (2020).
- [26] I. Frérot and T. Roscilde, Quantum critical metrology, *Phys. Rev. Lett.* **121**, 020402 (2018).
- [27] L. Garbe, M. Bina, A. Keller, M. G. A. Paris, and S. Felicetti, Critical quantum metrology with a finite-component quantum phase transition, *Phys. Rev. Lett.* **124**, 120504 (2020).
- [28] A. Niezgodą and J. Chwedeńczuk, Many-body nonlocality as a resource for quantum-enhanced metrology, *Phys. Rev. Lett.* **126**, 210506 (2021).
- [29] L. Garbe, O. Abah, S. Felicetti, and R. Puebla, Critical quantum metrology with fully-connected models: from heisenberg to kibble-zurek scaling, *Quantum Sci. Technol.* **7**, 035010 (2022).
- [30] K. Chen, J.-H. Lü, X. Zhu, H.-L. Zhang, W. Ning, Z.-B. Yang, and S.-B. Zheng, Critical sensing with a single bosonic mode without boson-boson interactions (2023), [arXiv:2305.17656](https://arxiv.org/abs/2305.17656) [quant-ph].
- [31] R. Liu, Y. Chen, M. Jiang, X. Yang, Z. Wu, Y. Li, H. Yuan, X. Peng, and J. Du, Experimental critical quantum metrology with the Heisenberg scaling, *npj Quantum Inf.* **7**, 170 (2021).
- [32] D.-S. Ding, Z.-K. Liu, B.-S. Shi, G.-C. Guo, K. Mølmer, and C. S. Adams, Enhanced metrology at the critical point of a many-body Rydberg atomic system, *Nat. Phys.* **18**, 1447 (2022).
- [33] M. Raghunandan, J. Wrachtrup, and H. Weimer, High-density quantum sensing with dissipative first order transitions, *Phys. Rev. Lett.* **120**, 150501 (2018).
- [34] T. L. Heugel, M. Biondi, O. Zilberberg, and R. Chitra, Quantum transducer using a parametric driven-dissipative phase transition, *Phys. Rev. Lett.* **123**, 173601 (2019).
- [35] S. Fernández-Lorenzo and D. Porras, Quantum sensing close to a dissipative phase transition: Symmetry breaking and criticality as metrological resources, *Phys. Rev. A* **96**, 013817 (2017).
- [36] T. Ilias, D. Yang, S. F. Huelga, and M. B. Plenio, Criticality-enhanced quantum sensing via continuous measurement, *PRX Quantum* **3**, 010354 (2022).
- [37] R. Di Candia, F. Minganti, K. V. Petrovnin, G. S. Paraoanu, and S. Felicetti, Critical parametric quantum sensing, *npj Quantum Inf.* **9**, 23 (2023).
- [38] Y. Chu, S. Zhang, B. Yu, and J. Cai, Dynamic framework for criticality-enhanced quantum sensing, *Phys. Rev. Lett.* **126**, 010502 (2021).
- [39] J.-H. Lü, W. Ning, X. Zhu, F. Wu, L.-T. Shen, Z.-B. Yang, and S.-B. Zheng, Critical quantum sensing based on the jaynes-cummings model with a squeezing drive, *Phys. Rev. A* **106**, 062616 (2022).
- [40] X. Zhu, J.-H. Lü, W. Ning, F. Wu, L.-T. Shen, Z.-

- B. Yang, and S.-B. Zheng, Criticality-enhanced quantum sensing in the anisotropic quantum Rabi model, *Sci. China Phys. Mech. Astron.* **66**, 250313 (2023).
- [41] K. Gietka, L. Ruks, and T. Busch, Understanding and Improving Critical Metrology. Quenching Superradiant Light-Matter Systems Beyond the Critical Point, *Quantum* **6**, 700 (2022).
- [42] E. Jaynes and F. Cummings, Comparison of quantum and semiclassical radiation theories with application to the beam maser, *Proc. IEEE* **51**, 89 (1963).
- [43] P. Alsing, D.-S. Guo, and H. J. Carmichael, Dynamic stark effect for the jaynes-cummings system, *Phys. Rev. A* **45**, 5135 (1992).
- [44] H. J. Carmichael, Breakdown of photon blockade: A dissipative quantum phase transition in zero dimensions, *Phys. Rev. X* **5**, 031028 (2015).
- [45] J. M. Fink, A. Dombi, A. Vukics, A. Wallraff, and P. Domokos, Observation of the photon-blockade breakdown phase transition, *Phys. Rev. X* **7**, 011012 (2017).
- [46] Q. Guo, S.-B. Zheng, J. Wang, C. Song, P. Zhang, K. Li, W. Liu, H. Deng, K. Huang, D. Zheng, X. Zhu, H. Wang, C.-Y. Lu, and J.-W. Pan, Dephasing-insensitive quantum information storage and processing with superconducting qubits, *Phys. Rev. Lett.* **121**, 130501 (2018).

Supplementary Material for “Critical quantum metrology robust against dissipation and non-adiabaticity”

Jia-Hao Lü,^{1,*} Wen Ning,^{1,*} Fan Wu,^{1,*} Ri-Hua Zheng,¹ Ken Chen,¹ Xin
Zhu,¹ Zhen-Biao Yang,^{1,2,†} Huai-Zhi Wu,^{1,‡} and Shi-Biao Zheng^{1,2,§}

¹*Fujian Key Laboratory of Quantum Information and Quantum Optics,
College of Physics and Information Engineering, Fuzhou University, Fuzhou, Fujian 350108, China*
²*Hefei National Laboratory, Hefei 230088, China*

CONTENTS

S1. Fisher information of the driven Jaynes-Cummings model	1
S2. Numerical simulations of the driven Xmon-resonator system	2
S3. Suppression of leakage to the second-excited state of the Xmon	2
S4. Correction of XY crosstalk	3
S5. Calibration of the signal field amplitude	5
S6. Observed photon-number distribution	5
References	6

S1. FISHER INFORMATION OF THE DRIVEN JAYNES-CUMMINGS MODEL

The population of the excited state $|e\rangle$ is defined as the expectation value of the excitation-number operator $P_e = |e\rangle\langle e|$. In the two-level approximation, the operator $|e\rangle\langle e|$ can be rewritten as $|e\rangle\langle e| = \frac{1}{2}(I + \sigma_z)$, where I denotes the identity operator and $\sigma_z = |e\rangle\langle e| - |g\rangle\langle g|$. Then the standard deviation of P_e is given by

$$\Delta P_e = \frac{1}{2} \sqrt{\langle (1 + \sigma_z)^2 \rangle - \langle 1 + \sigma_z \rangle^2} = \frac{1}{2} \sqrt{1 - \langle \sigma_z \rangle^2}. \quad (\text{S1})$$

Using the expression $\langle \sigma_z \rangle = 2P_e - 1$, we obtain

$$\Delta P_e = \frac{1}{2} \sqrt{1 - (2P_e - 1)^2} = \sqrt{P_e(1 - P_e)}. \quad (\text{S2})$$

For the dark state $|\phi_0\rangle$, $P_e = |c_-|^2 = \frac{1}{2}(1 - \sqrt{1 - \varepsilon^2})$. Substituting P_e into the above expression, we obtain $\Delta P_e = \varepsilon/2$. The corresponding Fisher information is defined as

$$\mathcal{F} = \frac{1}{P_e} \left(\frac{dP_e}{d\varepsilon} \right)^2 + \frac{1}{P_g} \left(\frac{dP_g}{d\varepsilon} \right)^2, \quad (\text{S3})$$

and is adopted in the main text. In the two-level approximation, $P_e + P_g = 1$. Then \mathcal{F} can be re-expressed as

$$\mathcal{F} = \left(\frac{1}{P_e} + \frac{1}{1 - P_e} \right) \left(\frac{dP_e}{d\varepsilon} \right)^2 = \frac{1}{P_e(1 - P_e)} \left(\frac{dP_e}{d\varepsilon} \right)^2. \quad (\text{S4})$$

* These authors equally contributed to the work.

† zbyang@fzu.edu.cn

‡ huaizhi.wu@fzu.edu.cn

§ t96034@fzu.edu.cn

Using $dP_e/d\varepsilon = \varepsilon/(2\sqrt{1-\varepsilon^2})$, we finally have

$$\mathcal{F} = \frac{1}{1-\varepsilon^2}. \quad (\text{S5})$$

On the other hand, the quantum Fisher information is [S1]

$$\mathcal{I} = 4[\langle \partial_\varepsilon \phi_0 | \partial_\varepsilon \phi_0 \rangle + \langle \partial_\varepsilon \phi_0 | \phi_0 \rangle^2] = \frac{1}{1-\varepsilon^2}, \quad (\text{S6})$$

which implies that the Cramér-Rao bound is saturated for all values of ε for our experimental measurements.

S2. NUMERICAL SIMULATIONS OF THE DRIVEN XMON-RESONATOR SYSTEM

In this section, we focus mainly on the influence brought about by the energy levels higher than the first excited state $|e\rangle$ of the qubit. For this purpose, we include the second excited state $|f\rangle$, while we note that the influences of the higher excited states on the system's dynamics are slight and can be neglected compared to $|f\rangle$. The Hamiltonian for the driven qutrit-resonator system is given by (setting $\hbar = 1$)

$$H = \omega_e |e\rangle\langle e| + (2\omega_e - \chi) |f\rangle\langle f| + \omega_r a^\dagger a + \Omega \left[a^\dagger \left(|g\rangle\langle e| + \sqrt{2}|e\rangle\langle f| + \frac{\varepsilon}{2} e^{-i\omega_s t} \right) + \text{H.c.} \right], \quad (\text{S7})$$

where a^\dagger and a denote the photonic creation and annihilation operators of the resonator with the frequency ω_r ; ω_e is the transition frequency between $|g\rangle$ and $|e\rangle$, and χ is the anharmonicity for the level ladder; Ω represents the qubit-boson interaction strength, and ε characterizes the rescaled amplitude of the microwave field coupled to the photonic mode with the frequency ω_s .

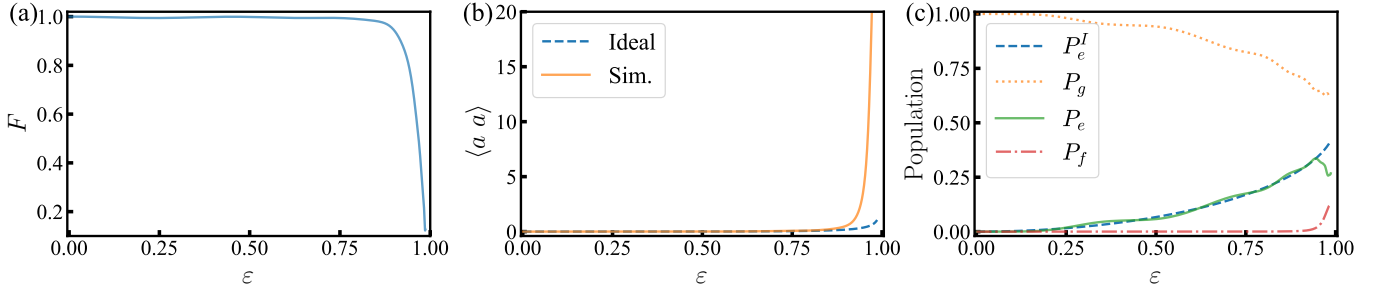


FIG. S1. The numerical simulations based on the Hamiltonian of Eq. (S7). (a) Fidelity of the qubit-resonator state to the ideal dark state as a function of ε . (b) The average photon number and (c) the qubit's population distribution as a function of ε . P_e^I denotes the $|e\rangle$ -state population of the ideal dark state. In the simulation, the parameters are the same as that shown in the main text.

We then perform the numerical simulations based on the Hamiltonian H in Eq. (S7). As shown in Fig. S1, when the resonator couples resonantly with both the qubit and the microwave field, the system's dynamics deviates significantly from the desired one when approaching the critical point, where the infidelity for the ideal dark state increases exponentially. Additionally, the average photon number exhibits a behavior that is very different from the ideal one near the critical point, owing to the large leakage to the bright states. Although the qubit's $|e\rangle$ -state population is insensitive to the leakage to the bright states in the two-level approximation, it presents an undesirable behavior near the critical point where the population of the $|f\rangle$ -state increases to 0.13. As shown in Fig. S1(c), the non-negligible influence of the $|f\rangle$ -state breaks down the monotonous feature of the $|e\rangle$ -state population near the critical point.

S3. SUPPRESSION OF LEAKAGE TO THE SECOND-EXCITED STATE OF THE XMON

To make the sensor work near the critical point, it is necessary to suppress the population of the second excited state of the Xmon. We find that this can be significantly optimized by fine tuning the detunings of the Xmon and the resonator from the signal field. With the detunings being included, the system Hamiltonian in the framework rotating at the frequency of the signal field is

$$H' = \Delta\omega_e |e\rangle\langle e| + (2\Delta\omega_e - \chi) |f\rangle\langle f| + \Delta\omega_r a^\dagger a + \Omega \left[a^\dagger \left(|g\rangle\langle e| + \sqrt{2}|e\rangle\langle f| + \frac{\varepsilon}{2} \right) + \text{H.c.} \right], \quad (\text{S8})$$

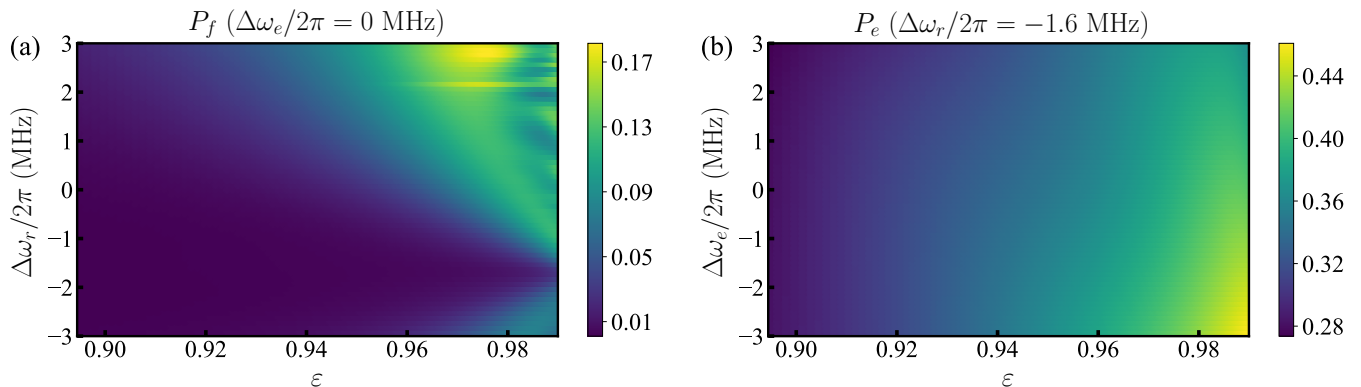


FIG. S2. The numerical simulations with the fine-tuned frequency detunings. (a) The qubit's $|f\rangle$ -state population versus the detuning of the resonator to the signal field during the evolution. It shows that the probability of leaking to the state $|f\rangle$ can be highly suppressed at a specific detuning. We here set the detuning between the qubit and the signal field to zero. (b) The qubit's $|e\rangle$ -state population versus the detuning of the qubit to the signal field. The detuning between the resonator and the microwave field is chosen as $-2\pi \times 1.6$ MHz. The other parameters are the same as shown above.

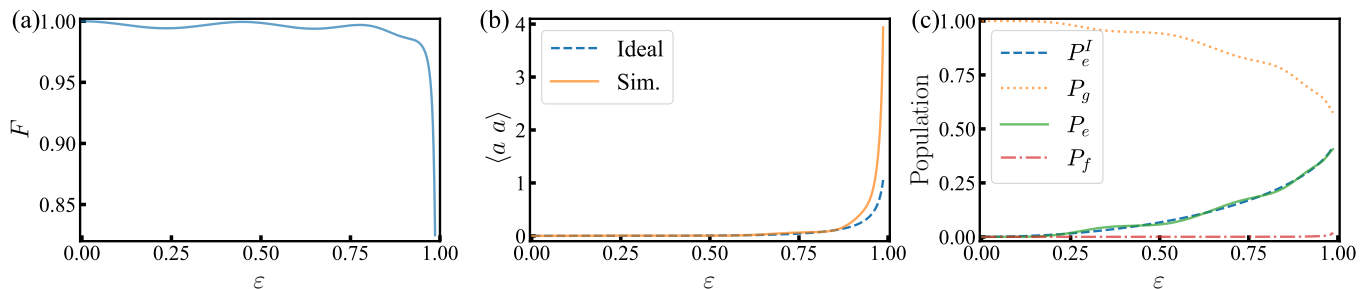


FIG. S3. The numerical simulations with the chosen frequency detunings. (a) Fidelity of the qubit-resonator state to the ideal dark state versus ε . (b) The average photon number and (c) the qubit's population distribution versus ε . P_e^I denotes the $|e\rangle$ -state population of the ideal dark state. In the simulation, the detunings of the resonator and the qubit with respect to the signal field are tuned to $-2\pi \times 1.6$ MHz and $2\pi \times 1.0$ MHz, respectively. The other parameters are the same as shown above.

where $\Delta\omega_r = \omega_r - \omega_s$ and $\Delta\omega_e = \omega_e - \omega_s$ are the detunings of the resonator and the qubit with respect to the signal field, respectively.

We then perform the numerical simulations by tuning $\Delta\omega_r$ and $\Delta\omega_e$ successively, as exhibited in Fig. S2, which shows that the probability of leaking to the $|f\rangle$ -state can be highly suppressed through the optimization of the frequency detunings, and the $|e\rangle$ -state population agrees well with that of the on-resonance dynamics. Seen from Fig. S2, we note that the set of optimal detunings of the resonator and the qubit with respect to the signal field are $-2\pi \times 1.6$ MHz and $2\pi \times 1.0$ MHz, respectively. With the chosen frequency detunings, when approaching the critical point we find that the fidelity with respect to the effective model remains higher than 0.9 for $\varepsilon = 0.98$; the associated average photon number is greatly reduced as compared to the case without such a frequency adjustment; and more importantly, the probability of leaking to the $|f\rangle$ -state decreases correspondingly such that the qubit's $|e\rangle$ -state population becomes well consistent with the ideal situation. In view of experiments, we further fine tune the detunings of the resonator and the qubit around the numerically estimated optimal parameters (i.e. $\Delta\omega_r = -2\pi \times 1.6$ MHz and $\Delta\omega_e = 2\pi \times 1.0$ MHz), making the overall evolution dynamics match the theoretical predictions (as elaborated in the main text).

S4. CORRECTION OF XY CROSSTALK

The superconducting circuit sample used in our experiment consists of five frequency-tunable Xmon qubits interconnected by a bus resonator, as described elsewhere [S2–S4]. Our experiment involves two of the qubits, one of which serves as the test qubit, labeled as Q_T , to establish the critical quantum dynamics together with the bus resonator, and the other, labeled as Q_A , to read out the photon number distribution of the resonator by observing its on-resonance Rabi signal. Additionally, we use the XY-control line of the qubit Q_R to apply a microwave drive to the resonator by crosstalk interactions. The remaining qubits are at their sweep points, so as to effectively decouple from the dynamics.

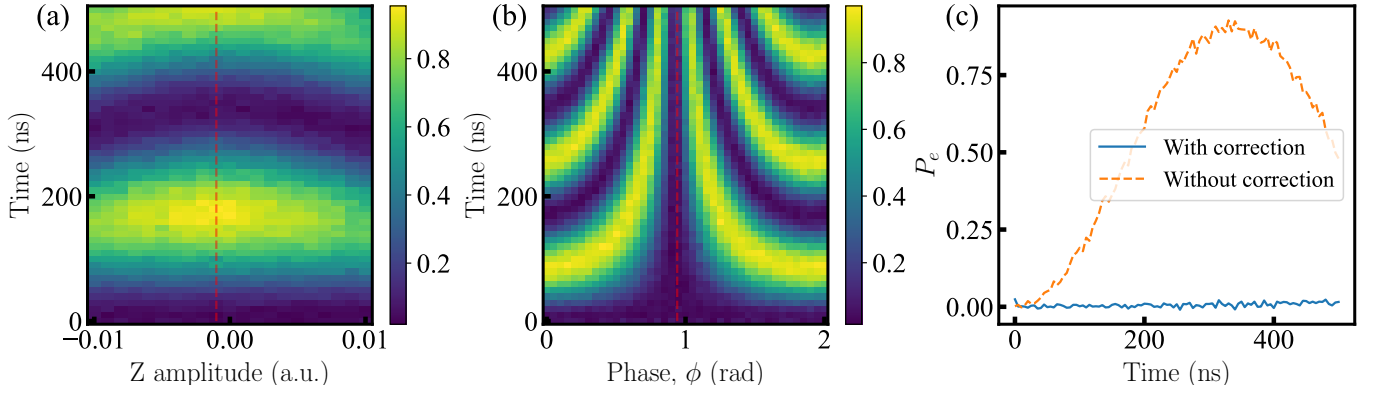


FIG. S4. Correction of the XY-crosstalk. (a) The measurement of the XY-crosstalk amplitude. A microwave pulse with frequency ω_I is applied to Q_R 's XY-control line after tuning Q_T to ω_I , generating a crosstalk Rabi oscillation on Q_T . The Rabi oscillations are measured with small deviation in frequency. The slowest Rabi oscillation corresponds to the crosstalk amplitude, as the red vertical dashed line shows. Here the pulse amplitude is set to $2\pi \times 5$ MHz. (b) The measurement of the XY-crosstalk phase. A microwave pulse with amplitude equal to crosstalk amplitude is added to Q_T 's XY-control line to cancel the crosstalk effect. The phase in which qubit is rarely excited is the crosstalk phase. (c) Experiment test for the crosstalk correction. With the applications of the XY-crosstalk correction, Q_T is barely excited. The pulse amplitude here is set to $2\pi \times 10$ MHz.

The pulse sequence of our experiment is shown in Fig. S6. When Q_T is tuned to couple resonantly with the resonator, the phase and the drive strength of the XY-drive crosstalks between Q_T and the resonator must be corrected [S5]. Figure S4 illustrates the calibration process for the XY-drive applied to the resonator as an example.

We start by calibrating the amplitude of the crosstalk, with the results shown in Fig. S4(a). For this, Q_T is biased to the frequency $\omega_I/2\pi = 5.53$ GHz, which is close to the resonator's frequency, and the other qubits are decoupled from Q_T and the resonator. It should be emphasised that the reason we are unable to perform the XY crosstalk calibration at the resonator's frequency is that the on-resonance dynamics between Q_T and the resonator complicates the effect of the crosstalk, which makes the crosstalk amplitude extremely difficult to capture. We here assume that a small frequency detuning has no effect on the crosstalk. After that, a strong flat-top-envelope microwave pulse is applied to the Q_R 's XY-control line with frequency ω_I , generating a crosstalk excitation on Q_T . The amplitude of the crosstalk of the resonator to Q_T can be obtained by fitting the slowest Rabi oscillation of the evolution of Q_T 's excitation, resulting from different frequency deviation in ω_I .

We characterize the phase of the crosstalk in terms of the frequency corresponding to the slowest Rabi oscillation in Fig. S4 (b). At this point, a microwave pulse with amplitude equal to the crosstalk amplitude of the resonator to Q_T , should be applied to Q_T to counteract the effect of the crosstalk. We then monitor the evolution of Q_T ' excitation for different phases of Q_T 's microwave pulse, with the π -phase of Q_R 's microwave pulse. As shown in Fig. S4 (b), Q_T is barely excited during the evolution process at a specific phase, meaning the phase difference of the XY-control lines of Q_R to Q_T .

The calibrations of Q_T to Q_R ' XY-control line are performed in the same way. To correct the crosstalks, we bias Q_T/Q_R to ω_I , and simultaneously apply on-resonance microwave pulses to them, with amplitudes A_1/A_2 and phases ϕ_1/ϕ_2 . During the process, the other qubits are effectively decoupled from these two qubits. However, owing to the effect of the crosstalks, the microwave's effect on each qubit at this point becomes

$$\begin{bmatrix} A_1 e^{i\phi_1} + A_{12} A_2 e^{i(\phi_{12} + \phi_2)} \\ A_2 e^{i\phi_2} + A_{21} A_1 e^{i(\phi_{21} + \phi_1)} \end{bmatrix} = \begin{bmatrix} 1 & A_{12} e^{i\phi_{12}} \\ A_{21} e^{i\phi_{21}} & 1 \end{bmatrix} \begin{bmatrix} A_1 e^{i\phi_1} \\ A_2 e^{i\phi_2} \end{bmatrix}, \quad (\text{S9})$$

where A_{jk} and ϕ_{jk} denote the crosstalk amplitude and phase of qubit k to qubit j , respectively, quantified by means of the method described above. This means that, to cancel the effect of the crosstalk, a corrected microwave pulse

$$\begin{bmatrix} 1 & A_{12} e^{i\phi_{12}} \\ A_{21} e^{i\phi_{21}} & 1 \end{bmatrix}^{-1} \begin{bmatrix} A_1 e^{i\phi_1} \\ A_2 e^{i\phi_2} \end{bmatrix}, \quad (\text{S10})$$

should be applied to get the expected microwave pulse.

To ensure the validity of the XY-crosstalk correction, we bias Q_T to ω_I and apply the corresponding calibrated microwave pulses to Q_R and Q_T , respectively. We then observe the evolution of Q_T ' excitation, as displayed in Fig. S4 (c). The result verifies the validity of such a correction.

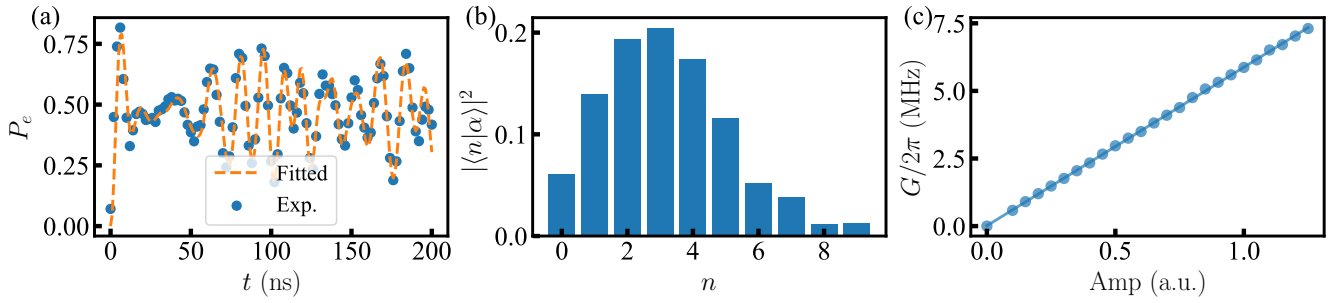


FIG. S5. Calibration of the drive strength of the microwave. (a) The experimental (dots), the fitted (solid line) Rabi oscillations and (b) the corresponding photon-number distribution of the resonator. Here, τ is set to 100 ns with a specific pulse amplitude of the microwave. (c) The drive strength G as a function of the pulse amplitude of the microwave.

S5. CALIBRATION OF THE SIGNAL FIELD AMPLITUDE

In our experimental protocol, a time-dependent transverse field should be applied to the resonator. It is necessary to calibrate the linear relation between the pulse amplitude of the microwave and the driving field strength of the resonator.

To this end, we first use the XY-control line of Q_R to apply a microwave drive with the amplitude ξ to the resonator by the crosstalk interaction, which produces an equivalent driving field strength G to drive the resonator. After a time τ , the state of the resonator can be described as

$$|R(\tau)\rangle = e^{-iG(a+a^\dagger)\tau}|R(0)\rangle = |\alpha\rangle, \quad (\text{S11})$$

where $|R(0)\rangle = |0\rangle$ denotes the initial state of the resonator, and $\alpha = -iG\tau$ represents the displacement coefficient. The average photon number $|\alpha|^2$ of such a coherent state can then be read out by switching off the drive and tuning Q_A to couple resonantly with the resonator (the details are described in the next part). After that, the corresponding driving field strength $G = |\alpha|/\tau$ can be deduced. A linear connection of the pulse amplitude of the microwave to the driving field strength of the resonator can be naturally fitted through the applications of different pulse amplitude of the microwave, as exhibited in Fig. S5.

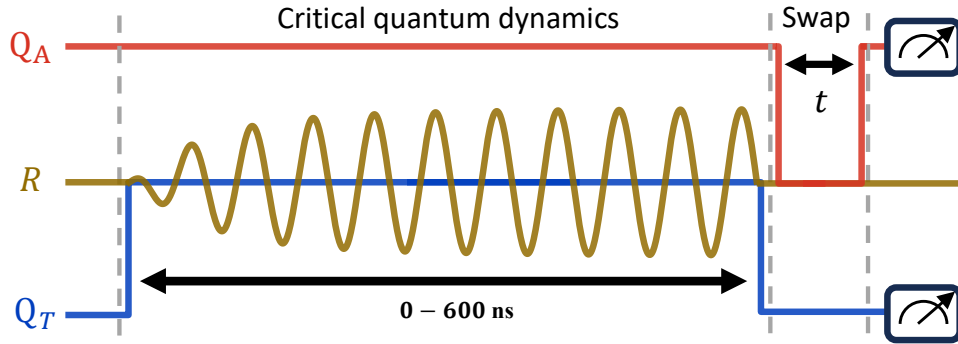


FIG. S6. Pulse sequence. The qubit (Q_T) is tuned from its frequency to the resonator's frequency. At the same time the signal field with a rescaled amplitude ε is coupled to the resonator. After the quench process, the qubit is biased back to its idle frequency for state readout, and the ancilla qubit (Q_A) is tuned to couple resonantly with the resonator to measure the photon-number distribution.

S6. OBSERVED PHOTON-NUMBER DISTRIBUTION

After the interaction dynamics between the qubit Q_T and the resonator, the transverse field is switched off, so that the qubit is effectively decoupled from the resonator. The photon number distribution of the resonator is read out by tuning the ancilla qubit Q_A , initially in its ground state, to the resonator frequency, and then observing its Rabi oscillations [S6]. The excited state population $P_e^\varepsilon(\tau)$ of Q_A , after tuning back to its idle frequency, for the rescaled amplitude ε at the evolution time τ is measured, the pulse sequence is shown in Fig. S6. The measured average photon numbers are calculated by the photon-number distribution, which is fitted by the time-dependent Rabi signal as

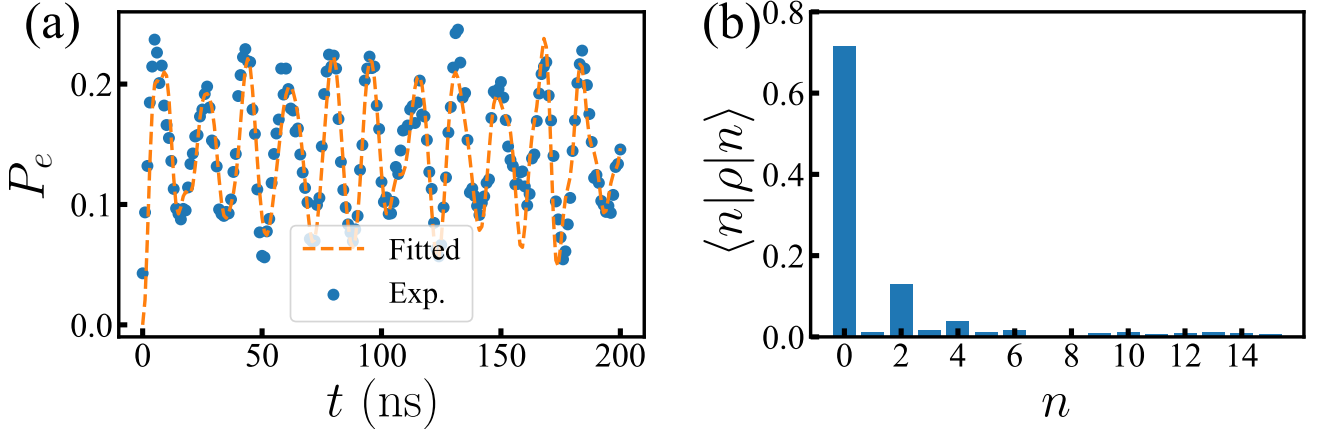


FIG. S7. (a) The experimental (dots), the fitted (solid line) Rabi oscillations and (b) the corresponding photon-number distribution of the resonator with $\varepsilon = 0.964$.

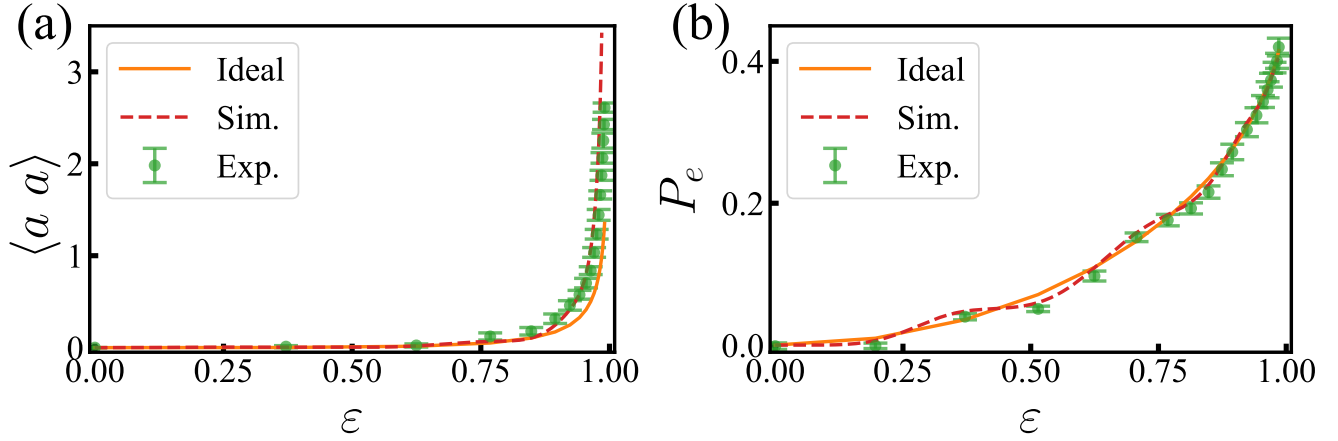


FIG. S8. (a) The experimental average photon number and (b) the $|e\rangle$ -state population as a function of ε during the whole dynamics. The solid lines denote the result of the ideal dark state, and the dashed lines are that for the numerical simulations.

$$P_e^\varepsilon(\tau) = \frac{1}{2} \left[1 - P_g^\varepsilon(0) \sum_{n=0}^{n_{max}} P_n e^{-\kappa_n \tau} \cos(2\sqrt{n}\Omega_A \tau) \right], \quad (\text{S12})$$

where $P_g^\varepsilon(0)$ denotes the probability for Q_A initially in its ground state, P_n presents the probability for the $|n\rangle$ -state photon-number distribution, n_{max} is the fitted cutoff of the photon number, $\kappa_n = n^l/\kappa_r$ ($l = 0.7$) is the empirical decay rate of the $|n\rangle$ -state Rabi oscillation and Ω_A represents the on-resonance photonic swapping rate between Q_A and the resonator. Here, the ideal dark state of the resonator is a squeezed vacuum state, which means that the high-photon state distribution affects the dynamics markedly, increasing the difficulty of the fitting. The measured time-dependent Rabi oscillation signal and its fitting are shown in Fig. S7(a). The corresponding photon-number distribution is presented in Fig. S7(b).

In Fig. S8, we present the average photon number of the resonator and the $|e\rangle$ -state population of Q_T during the whole dynamics. As expected, the qubit's excitation number is robust against the imperfect system dynamics rather than the average photon number, making P_e serve as an ideal indicator for critical quantum sensing.

[S1] L. Garbe, M. Bina, A. Keller, M. G. A. Paris, and S. Felicetti, Critical Quantum Metrology with a Finite-Component Quantum Phase Transition, *Phys. Rev. Lett.* **124**, 120504 (2020).

[S2] S. Chao, et al., Continuous-variable geometric phase and its manipulation for quantum computation in a superconducting circuit, *Nat Commun.* **8**, 1061 (2017).

- [S3] W. Ning et al., Deterministic Entanglement Swapping in a Superconducting Circuit, *Phys. Rev. Lett.* **123**, 060502 (2019).
- [S4] R.-H. Zheng et al., Observation of a Superradiant Phase Transition with Emergent Cat States, *Phys. Rev. Lett.* **131**, 113601 (2023).
- [S5] K. Xu et al., Probing Dynamical Phase Transitions with a Superconducting Quantum Simulator, *Sci. Adv.* **6**, eaba4935 (2020).
- [S6] M. Hofheinz et al., Synthesizing Arbitrary Quantum States in a Superconducting Resonator, *Nature* **459**, 546 (2009).